



Convergent Richtmyer–Meshkov turbulence by time-resolved planar laser-induced fluorescence measurement

Yong Zhao¹, Juchun Ding^{1,2} , Dong He¹, Zhangbo Zhou¹  and Xisheng Luo¹ 

¹Department of Modern Mechanics, University of Science and Technology of China, Hefei 230026, PR China

²Laoshan Laboratory, Qingdao 266237, PR China

Corresponding authors: Juchun Ding, djc@ustc.edu.cn; Xisheng Luo, xluo@ustc.edu.cn

(Received 16 October 2024; revised 9 January 2025; accepted 9 January 2025)

We report the first measurement of turbulent mixing developing from the convergent Richtmyer–Meshkov (RM) instability using time-resolved planar laser-induced fluorescence in a semi-annular convergent shock tube. A membraneless yet sharp interface with random short-wavelength perturbations, but controllable long-wavelength perturbations, is created by an automatically retractable plate, enhancing the reproducibility and reliability of RM turbulence experiments. The cylindrical air/SF₆ interface formed is first subjected to a convergent shock, then to its reflected shock and subsequently transits to turbulent mixing. It is found that the mixing width after reshock has a linear growth rate more than twice the rate in planar geometry. Also, the mixing width does not present power-law growth at late stages as in a planar geometry. However, the scalar spectrum and transition criterion obtained are similar to their planar counterparts. These findings indicate that the geometric constraint greatly affects the large scales of the flow, while having a weaker effect on the small scales. It is also found that the reflected shock significantly increases both scale separation and Reynolds number, explaining the rapid transition to turbulence following reshock.

Key words: shock waves, nonlinear instability, turbulent mixing

1. Introduction

When a corrugated interface separating two different fluids is accelerated by a shock wave, initial perturbations on the interface grow first linearly, then nonlinearly over time, potentially leading to a transition to turbulent mixing. This phenomenon is usually referred to as Richtmyer–Meshkov (RM) instability (Richtmyer 1960; Meshkov 1969). A similar yet distinct phenomenon is Rayleigh–Taylor (RT) instability, which occurs as the interface

suffers continuous acceleration from a lighter fluid to a heavier one (Rayleigh 1883; Taylor 1950). Turbulence induced by RM instability is a hot topic in fundamental research, including compressible turbulence, and also plays an important role in applications such as inertial confinement fusion (ICF) (Lindl *et al.* 2014).

The RM turbulence is unsteady, inhomogeneous and anisotropic, posing significant challenges to flow diagnostics. Planar laser-induced fluorescence (PLIF) and particle image velocimetry (PIV) have proven to be promising techniques for measuring the RM turbulence (Sewell *et al.* 2021). The first application of PLIF diagnostic to RM instability experiment was reported by Jacobs (1992). The results showed that PLIF can not only capture fine-scale structures but also enable the quantitative measurement of the gas concentration distribution. Later, simultaneous PLIF-PIV measurements were achieved by Balakumar *et al.* (2008), which greatly facilitates the RM turbulence research (Mohaghar *et al.* 2019). In recent years, advancements in high-frequency lasers and high-speed cameras have led to the development of high-frequency PLIF, PIV and simultaneous PLIF-PIV techniques. Carter *et al.* (2019) presented novel measurements of RM turbulence using simultaneous PLIF-PIV photography at 60 kHz, enabling a detailed analysis on non-stationary physics. Noble *et al.* (2020) conducted the 20 kHz PLIF measurement of RM turbulence, and found that the statistical moments of the mole fraction are consistent with the results of turbulent jet experiments. More recently, time evolutions of kinetic and scalar energy spectra in RM turbulence were obtained using simultaneous PLIF-PIV measurements at 20 kHz (Noble *et al.* 2023). However, existing experiments are limited to the RM turbulence triggered by a planar shock.

The convergent RM instability, which involves an initial setting more relevant to ICF, has become increasingly attractive in recent years. Several types of convergent shock tubes have been developed to facilitate experiments on convergent RM instability (Hosseini & Takayama 2005; Biamino *et al.* 2015; Luo *et al.* 2018). However, these convergent shock tubes typically possess complex structures that hinder the implementation of PLIF and PIV measurements, limiting existing experiments to schlieren and shadow diagnostics. Therefore, a novel convergent shock tube optimized for PLIF or PIV diagnostics is highly desired for RM turbulence experiments. In addition, the development of RM turbulence is sensitive to initial conditions of the interface, indicating that the interface formation is crucial. Generally, there are two types of interface formation technique. One is the membraneless technique, which inevitably introduces uncontrollable long-wavelength perturbations and a diffusion layer on the interface, both of which significantly influence turbulence evolution (Wang *et al.* 2022). An alternative technique is using a membrane or soap film to physically separate two different gases (Biamino *et al.* 2015). However, membrane fragments or soap droplets generated by the shock impact can significantly contaminate the turbulence field and also impede PLIF and PIV diagnostics. Due to these limitations, quantitative measurements of convergent RM turbulence have not yet been achieved in shock-tube experiments. So far, main characteristics of convergent RM turbulence (such as statistics evolution and transition criterion), along with its differences from the planar counterpart, remain unknown. These motivate the present study.

In this work, we will investigate the turbulent mixing arising from the convergent RM instability in a semi-annular shock tube. A novel automatically retractable plate, controlled by electromagnetic force, is designed to create a cylindrical, membraneless and sharp interface. Time-resolved PLIF diagnostic is adapted to the convergent shock tube, realizing the turbulence field measurement. Evolutions of statistics such as mixing layer width, mixedness parameter, scalar energy spectrum and turbulent length scales are analysed to show the characteristics of the convergent RM turbulence. Main differences between the convergent RM turbulence and its planar counterpart are discussed.

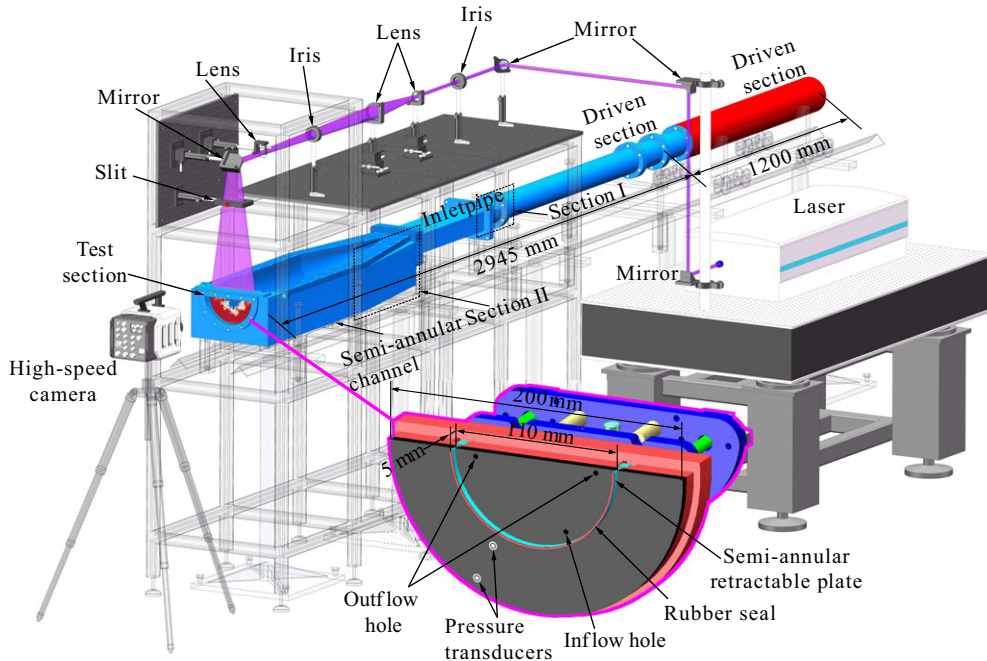


Figure 1. Schematic of the semi-annular shock tube, the time-resolved PLIF system and the interface formation device.

2. Experimental methods

The experiments are performed in the semi-annular shock tube originally designed by Luo *et al.* (2015). The reproducibility and reliability of the facility for generating convergent shock waves have been thoroughly verified (Ding *et al.* 2017*b*). A schematic diagram of the shock tube is given in figure 1. An incident planar shock is first formed in the driven section by suddenly rupturing the polypropylene diaphragm between the driver and driven sections. As the shock passes through the transformation section I and travels in the inlet pipe, the circular shock transitions into a semi-circular one. Subsequently, the shock passes through the transformation section II and moves in the semi-annular channel as a semi-annular one. Finally, the shock propagates to the test section and turns into a semi-cylindrical shock. Benefiting from the semi-cylindrical structure of the facility, a silica glass panel can be installed on top of the test section, enabling the laser sheet to enter for PLIF measurement. A lamp-pumped pulsed Q-switched Nd:YAG laser (SGR, Beamtech limited) is used to create a pulse train (30 pulses) at a repetition rate of 12.5 kHz. For each pulse, the fourth harmonic output at 266 nm with an average energy of 100 mJ is used. The output beam is directed into mirrors and lenses, and finally becomes a diverging laser sheet with a thickness of 0.5 mm at the beam waist. The laser sheet excites the acetone premixed with SF₆ (test gas) inside the test section, producing fluorescence with a peak at 420 nm. The fluorescence is captured by a high-speed camera (TMX7510, Phantom Limited), synchronized with the laser timing at a frequency of 12.5 kHz. The camera has a spatial resolution of 0.17 mm per pixel and a shutter time of 1 μ s. The ambient pressure and temperature are 101.3 ± 0.1 kPa and 297.4 ± 0.2 K, respectively.

Initial imperfections on the interface, such as diffusion layers, membrane fragments and soap droplets, could significantly affect RM turbulence. To mitigate these

undesired factors, an automatically retractable plate is designed to create a cylindrical, membraneless, sharp interface with random short-wavelength perturbations and controllable long-wavelength perturbations. As depicted in [figure 1](#), a semi-cylindrical device, which consists of a retractable plate, an electromagnet and two springs, is inserted into the test section from the inner side. When the electromagnetic coil is energized, an electromagnetic force is generated, causing the plate to come into contact with the viewing glass on the outer side. The extension length of the plate is 5.0 mm, matching the inner height of the test section. Its leading edge is equipped with a soft rubber seal, enabling a gentle contact between the plate and the glass while also preventing gas diffusion. Later, the binary mixture of SF₆ and vapourized acetone is injected into the region enclosed by the protruding plate through an inflow hole, while air is exhausted through two outflow holes. When the incident shock is about to reach the test section (detected by a pressure transducer), the electromagnetic force is deactivated, allowing the plate to retract under the pulling force of the springs. This process creates a membraneless air/SF₆ interface with a relatively sharp profile. Note the plate moves at an average speed of 0.4 m s⁻¹, which is negligible compared with the shock-induced velocity. Therefore, the shear flow in the spanwise direction has a negligible effect on the perturbation growth. The retraction introduces random short-wavelength perturbations at the interface, serving as initial seeds for the RM turbulence in this study. More importantly, this technique avoids the uncontrollable long-wavelength perturbations and diffusion layers present in previous experiments (Noble *et al.* 2023), significantly enhancing the reproducibility and reliability of the RM turbulence experiments. The long-wavelength perturbations on the interface can be accurately controlled by changing the plate shape. As the first experiments, a cylindrical plate is utilized in this work to create a cylindrical air/SF₆ interface with random short-wavelength perturbations.

3. Results and discussion

Three experimental runs (corresponding to cases 1–3) are performed in this work. Initial conditions are listed in [table 1](#). The Atwood number (A) is defined as $A = (\rho_2 - \rho_1) / (\rho_2 + \rho_1)$ with ρ_1 (ρ_2) being the gas density on the exterior (interior) side of the interface, and the mass fraction of SF₆ is calculated based on one-dimensional (1-D) gas dynamics theory. The main steps for converting PLIF images from intensity to mole fraction are outlined below. First, the distortion caused by the camera system is corrected using a circular calibration plate. Next, background images (taken without the injection of the SF₆ and acetone mixture into the test section) are subtracted from the PLIF images. Then, the divergence and spatial variation of the laser sheet are taken into account. Also, Beer's law attenuation is iteratively calibrated under the assumption of adiabatic mixing. Finally, a notch filter is applied to remove striations caused by interface refraction. After this process, the mole fraction of the gas mixture, rather than just SF₆, enclosed by the interface is obtained.

The initial interface formed in the present experiments is relatively sharp, enabling the extraction of the isoline where the mole fraction of the interior gas is 0.5, as depicted in [figure 2\(a\)](#), where the dash-dotted lines represent the average position of the initial interface. The perturbations in cases 1 and 3 are nearly identical, which explains the similar growth rate of mixing width observed later. In contrast, the amplitude of case 2 is relatively smaller, but its phase aligns with those of cases 1 and 3. For spherical RM instability, spherical harmonics are typically employed to initialize interfacial perturbations, as they effectively avoid the pole singularity problem on a spherical interface (Lombardini, Pullin & Meiron 2014). However, for RM instabilities in cylindrical geometries, which are

Case	Ma	h_0 (mm)	R (mm)	$m_{\text{fra}}(\text{SF}_6)$	A	χ_{acetone} (%)
1	1.26	2.98	54.9	0.88	0.53	4.5
2	1.25	2.51	54.7	0.89	0.54	4.4
3	1.26	2.93	54.9	0.88	0.53	4.4

Table 1. Initial conditions for cases 1–3. Ma : Mach number of the incident shock when it arrives at the interface; R : radius of initial interface; h_0 : initial width of the mixing layer; $m_{\text{fra}}(\text{SF}_6)$: SF_6 mass fraction; A : Atwood number; χ_{acetone} : acetone volume fraction.

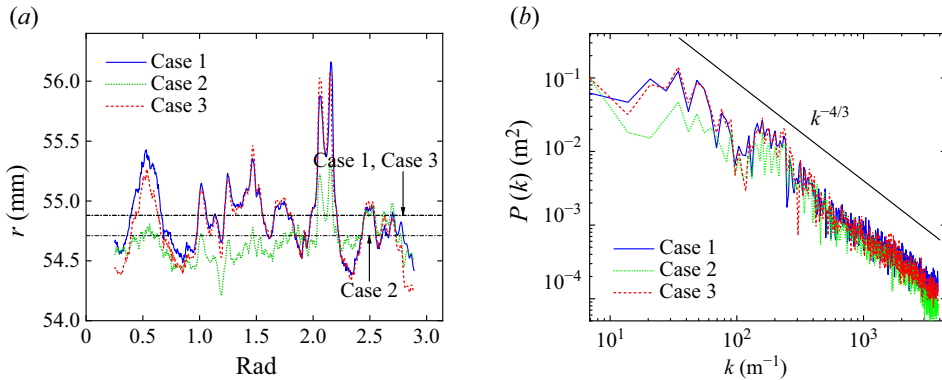


Figure 2. (a) The radial position of the initial interface plotted against the azimuthal angle. The dash-dotted lines indicate the average position of the initial interface. (b) The power spectra of the initial perturbations. The black line serves as a reference for a scaling law.

simpler than spherical geometries, a linear superposition of Fourier harmonics is more commonly recommended (Ge *et al.* 2020). In the present experiments, the initial interface is measured on a 2-D plane using PLIF diagnostics, and thus the amplitude of the initial perturbations can be expanded as

$$f(\theta) = \sum_{m=0}^N f_m e^{ik_m R \theta}, \quad (3.1)$$

where the amplitude coefficients f_m are determined by the variance $\sigma_m^2 = (1/2\pi)((P(k_m)/k_m))\Delta k$ with $P(k_m)$ being the power spectrum. Figure 2(b) displays the power spectra of the initial perturbations for cases 1–3. It is evident that the retractable plate generates a specific multi-mode perturbation characterized by small amplitudes across a broad range of high wavenumbers. The perturbation spectrum exhibits an approximate scaling law of $-4/3$, similar to observations in ICF capsules (Barnes *et al.* 2002).

Evolutions of mole fraction field for cases 1–3 are displayed in figure 3. Time origin is set at the moment when the incident shock encounters the interface. The first row of images illustrates the initial interface, while the second row displays the interface after the shock impact. Fine-scale interface structures at every stage are clearly captured by the PLIF diagnostic. Unlike previous experiments, the interface here maintains a distinct and sharp morphology during both the linear and nonlinear stages, indicating the elimination of diffusion layer on the initial interface formed. Moreover, large-scale perturbations along the cylinder axis caused by the retracting plate are effectively excluded in the

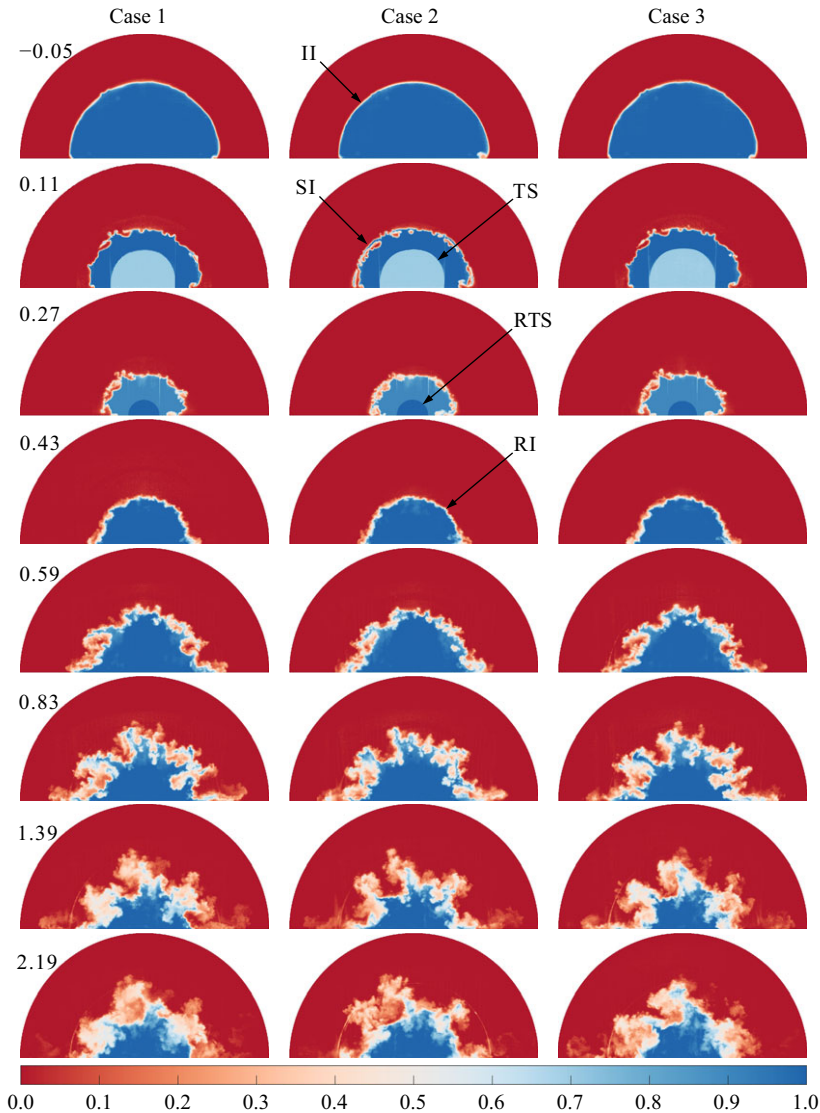


Figure 3. Temporal evolutions of mole fraction distribution for cases 1–3. II, initial interface; SI, shocked interface; TS, transmitted shock; RTS, reflected transmitted shock; RI, reshocked interface. Numbers at the top left of the images in the first column are in time (unit: ms).

present experiments. According to our previous study (Ding *et al.* 2017a), if large-scale perturbations are present along the cylinder axis, the longitudinal interface will evolve rapidly with the roll-up of vortices following shock impact, resulting in significant mutual penetration of flow structures between planes perpendicular to the cylinder axis. However, the present experimental results show no such mutual penetration, providing evidence against the presence of large-scale perturbations. As the shocked interface moves inward, the short-wavelength perturbations produced by the retracting plate grow rapidly. Later, the transmitted shock focuses at the convergence centre, immediately generating a diverging reflected shock (0.27 ms). Subsequently, this reflected shock re-impacts the evolving interface, leading to a rapid transition to turbulent mixing ($t > 0.59$ ms). The laminar

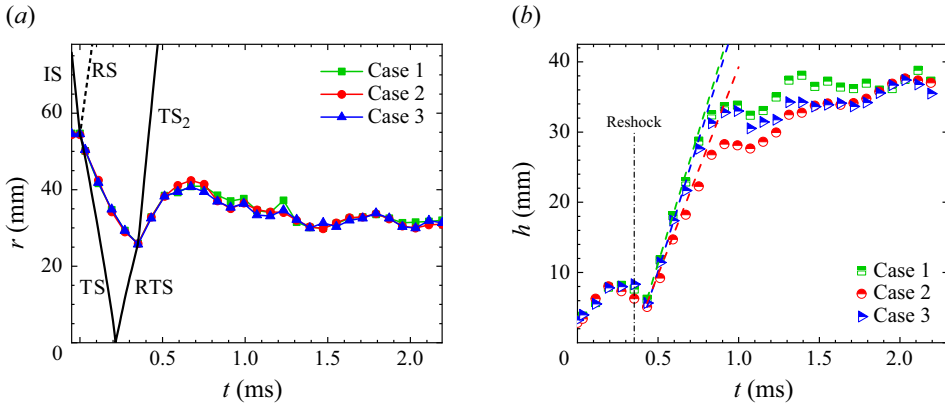


Figure 4. (a) Trajectories of the interface and shock waves and (b) the mixing layer width vs. time for cases 1–3. Dashed lines in (b) indicate the linear fits of data. IS, incident shock; TS₂, second transmitted shock. The other symbols are the same as those in figure 3.

boundary layer in the post-shock flow has a maximum thickness of 0.11 mm, indicating that it has a negligible influence on the interface development. If the laminar boundary layer transitions to turbulence after reshock (similar to the main flow), the turbulent boundary layer is not expected to be an order of magnitude thicker than the laminar boundary layer (i.e. 1.1 mm) during the short experimental period. The PLIF diagnostic captures the flow information at the centre plane of the test section (2.5 mm from either wall). Therefore, the flow field captured by PLIF cannot be significantly affected by the boundary layer.

An $r-t$ diagram illustrating the trajectories of the interface and shock waves is given in figure 4(a). The wave motions are calculated with 1-D gas dynamics theory, which can approximately represent the actual shock propagation process. The interface position is extracted from the mole fraction image where $\langle \xi \rangle = 0.5$, with $\langle \cdot \rangle$ denoting the circumferential averaging. In general, the interface trajectories for cases 1–3 are similar. Impacted by the incident shock, the interface moves inwards at an initial velocity of approximately 110.0 m s^{-1} . Then, it experiences evident deceleration, consistent with previous schlieren results (Ding *et al.* 2017b). Following reshock, the interface first undergoes a short period of outward motion, then decelerates and even moves inwards gradually due to mass conservation of the fluid enclosed by the interface. This confirms the numerical results of Lombardini *et al.* (2014). Visible oscillations in the interface trajectory are observed, which is ascribed to the subsequent waves reverberating between the interface and geometric centre.

The growth of the mixing layer width is plotted in figure 4(b). The mixing width is defined as $h = r_s - r_b$ with r_s being the radius where the average mole fraction of heavy gas $\langle \xi \rangle = 0.05$ and r_b being the radius where $\langle \xi \rangle = 0.95$. After the incident shock impact, the mixing width exhibits a rapid growth ($t < 0.2 \text{ ms}$). Later, the growth rate suffers a continuous drop and even becomes negative due to the RT stabilization effect caused by interface deceleration (Ding *et al.* 2017b). After reshock, the mixing width first suffers a sudden drop due to shock compression, then presents a period of quasi-linear growth with time. Such a quasi-linear growth is qualitatively consistent with the behaviour of reshocked RM instability in planar geometry (Leinov *et al.* 2009). Mikaelian (1989) has proposed an empirical model to predict the mixing width growth for RM turbulence

$$\frac{dh}{dt} = C_M \Delta V |A_r^+|, \quad (3.2)$$

where ΔV is the interface jump velocity caused by reshock, A_r^+ is the post-reshock Atwood number and C_M is an empirical coefficient. Performing a linear fit of the present data, C_M is found to be 0.99, 0.83 and 0.98 for cases 1–3, respectively. Note that $C_M = 0.28$ is suggested by Mikaelian (1989), and $C_M = 0.28 \sim 0.39$ is suggested by experiments on planar RM instability with reshock (Leinov *et al.* 2009). This means that the present growth rate in the convergent geometry is more than twice the rate in planar RM turbulence. The explanation is as follows. The interface experiences unsteady motion in a convergent geometry, triggering RT instability or stability, which may be a key factor for the quicker growth of perturbations. As we know, the RT instability occurs when the acceleration vector is directed from a light fluid toward a heavy fluid. To identify these periods in our experiment, we calculate the interface acceleration by taking the second derivative of the interface trajectory given in figure 4(a). While our experimental time resolution limits precise quantification of instantaneous interface acceleration, qualitative analysis reveals that, following reshock ($t > 0.35$ ms), the outward-moving interface experiences deceleration due to mass conservation of the fluid enclosed by the interface. This deceleration triggers RT instability, which remains active until $t = 0.83$ ms, coinciding with the period of rapid quasi-linear growth observed in figure 4(b) between 0.43 and 0.83 ms. Additionally, geometric contraction enhances instability growth at an inward-moving interface, leading to a larger perturbation amplitude prior to reshock. This can also contribute to faster instability growth after reshock. Furthermore, unlike in previous planar experiments, the interface here lacks a diffusion layer, allowing it to retain a sharper morphology at the reshock moment. As noted by Ukai, Balakrishnan & Menon (2011), in such cases, more baroclinic vorticity is generated at the interface, further accelerating the instability growth. It is also found that, unlike the planar counterpart, the mixing width here does not exhibit a power-law growth at late stages. One major reason for this discrepancy is that the geometric centre restricts the mixing width growth. Also, subsequent waves reverberating between the interface and geometric centre also influence the mixing width growth.

The normalized mixed mass, defined as $\Psi = (\int \langle \rho \xi (1 - \xi) \rangle dr) / (\int \langle \rho \rangle \langle \xi \rangle \langle 1 - \xi \rangle dr)$ (Zhou, Cabot & Thornber 2016), is calculated to quantify the mixing degree within the mixing zone. Here, $\Psi = 1$ represents a homogenized molecular mixing, while $\Psi = 0$ represents a completely entrained flow. As seen in figure 5(a), there exists only a minor difference among the three cases, demonstrating high reproducibility of the present experiments. After the shock impact, Ψ experiences a rapid decay due to the growth of the mixing width. Later, RT stabilization effect begins to act, which suppresses the mixing width growth (i.e. erases the large-scale intrusion between the two gases), leading to a continuous rise in Ψ . It is seen that Ψ reaches a peak at the time of reshock. After reshock, nonlinearity becomes strong and bubble merging dominates the instability development, generating shorter-wavelength structures (see figure 3). This process leads to a continuous drop of the mixedness parameter to a valley. At late stages, turbulent transport becomes strong, causing Ψ to rise to the range 0.8–0.9. Other mixedness parameters including molecular mixing fraction Θ and mixing parameter \mathcal{E} (Cook & Dimotakis 2001) are also calculated, and they present a similar variation trend as Ψ .

The scalar energy spectra at moments after reshock are given in figure 5(b). They are calculated as follows. First, scalar fluctuations are obtained as $\xi^* = \xi - \langle \xi \rangle$. Then, these fluctuations are Fourier transformed and multiplied by their Fourier conjugates to derive the scalar energy spectrum across different radii

$$E(k) = F(\xi^*) F^{conj}(\xi^*). \quad (3.3)$$

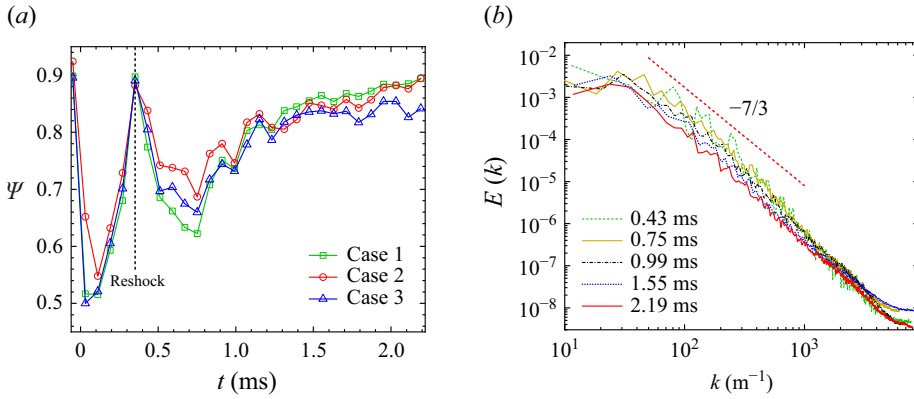


Figure 5. (a) Variations of mixedness with time for cases 1–3 and (b) the scalar energy spectra at times after reshock for case 1.

Finally, the scalar energy spectrum is obtained by spatially averaging within the inner mixing zone. It is important to note that the limited height of the test section introduces geometric constraints that become significant as the mixing width approaches the test section height. This confinement effect is characterized by the suppression of vortex stretching due to the narrow test section height, which potentially causes an inverse transfer of energy from small to large scales (Thorner & Zhou 2015). However, as depicted in figure 5(b), immediately following reshock, only a minor amount of energy is transferred to the long-wavelength region (between 0.43 and 0.75 ms). Subsequently, the scalar energy in the long-wavelength region undergoes a continuous decay, indicating the dominance of energy transfer to smaller scales in the present experiments. This phenomenon explains the sustained increase in mixedness observed at later stages in figure 5(a). Additionally, a distinctive feature of 2-D turbulence is the presence of an inertial subregion with a -3 scaling law at high wavenumbers (Boffetta & Ecke 2012). In contrast, the present results exhibit an inertial subrange with a $-7/3$ power law. According to Noble *et al.* (2023), for planar RM turbulence with $Sc = 0.7$ (the Schmidt number in the present experiments), the power-law slope ranges between -2.0 and -2.5 . The similarity between the present power-law slope and the planar counterpart suggests that the dynamics of small scales is not fundamentally affected by the limited test section and the layer's curvature. It is noteworthy that the scalar energy spectrum after reshock undergoes a slight change and displays a partial temporal similarity, but lacks strict self-similarity due to reverberating waves and geometric constraints. This behaviour, also observed in planar reshock RM turbulence (Tritschler *et al.* 2014), is interpreted as the rapid destruction of the initial conditions and large-scale structures following reshock. The present analysis indicates that although geometric constraints influence the flow evolution, they do not fundamentally alter the underlying mixing dynamics.

Turbulent length scales are measured within the mixing zone based on the mole fraction field. Because the turbulent length scales of cases 1–3 are similar, only the results for case 1 are shown here (the remaining results can be found in the Supplemental file). The Taylor microscale is calculated by $\lambda_T = \sqrt{\lambda_{T,r}^2 + \lambda_{T,\theta}^2}$ with the radial Taylor microscale $\lambda_{T,r}$ and the circumferential Taylor microscale $\lambda_{T,\theta}$ obtained from the spatial variance and gradients of the mole fraction fluctuation (Pope 2000). The Liepmann–Taylor scale, λ_L , is estimated based on the Taylor microscale as $\lambda_L \simeq 2.17\lambda_T$ (Dimotakis 2000). The Batchelor scale λ_B cannot be obtained directly from experiment due to the limited image

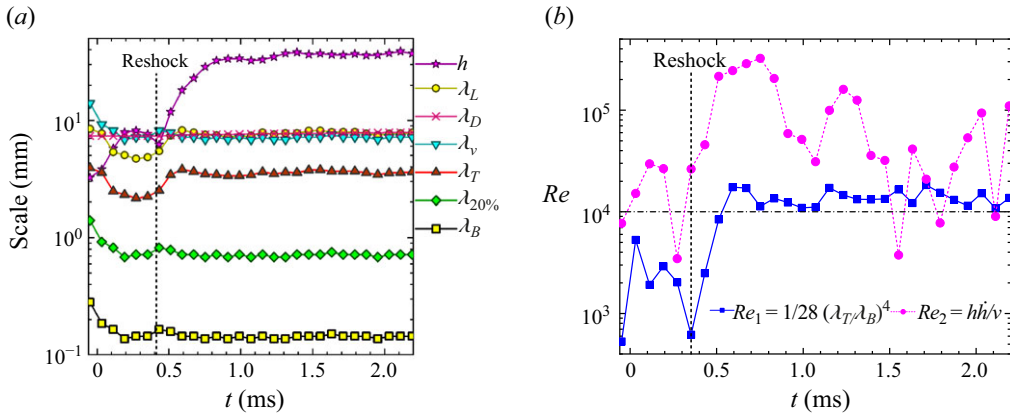


Figure 6. Evolutions of (a) turbulent length scales and (b) Reynolds numbers.

resolution, and is estimated from the dissipation layer thickness, i.e. $\lambda_{20\%} \simeq 5.0\lambda_B$ (Weber *et al.* 2014). In this work, $\lambda_{20\%}$ is calculated from the scalar dissipation rate field, representing the characteristic dissipation scale with the highest probability density. Since the Schmidt number $Sc \approx 0.7$ in the present experiments, λ_B is nearly equivalent to the Kolmogorov scale. Thus, the inner viscous scale, λ_v , can be estimated based on Batchelor scale as $\lambda_v \simeq 50\lambda_B$. For evaluating the flow transition, Dimotakis (2000) has proposed a criterion: $\lambda_L/\lambda_v > 1$. Later, Zhou *et al.* (2003b) proposed a new transition criterion, $\min(\lambda_D, \lambda_L) > \lambda_v$, for unsteady flow transition which additionally requires a sufficiently long evolution time. Here, the diffusion layer scale is $\lambda_D = 5(\nu t)^{1/2} + W_0^{r+}$, with ν being the kinematic viscosity and W_0^{r+} being the post-reshock mixing width (Groom & Thornber 2021). As shown in figure 6(a), both λ_L and λ_D are slightly larger than λ_v after reshock, indicating the establishment of an inertial subrange (i.e. the occurrence of mixing transition) after reshock. The present result illustrates that reshock causes a rapid flow transition to turbulent mixing by enhancing the scale separation.

The transition criterion in terms of Reynolds number is $Re > 1 - 2 \times 10^4$ (Dimotakis 2000). An outer-scale Reynolds number is calculated based on scale separation: $\lambda_L/\lambda_v = (1/10)Re_1^{1/4}$. Another definition of outer-scale Reynolds number is $Re_2 = h\dot{h}/\nu$. Notably, Re_2 is larger than Re_1 , as Re_2 is more sensitive to the evolution of large-scale structures, while Re_1 , calculated on the turbulent integral scale, remains largely unaffected. As plotted in figure 6(b), both Reynolds numbers experience a rapid growth after reshock. This observation is consistent with the enhancement of scale separation caused by reshock. The present finding explains the quick transition after reshock seen in both previous and current experiments. It is found that both Re_1 and Re_2 are greater than 1×10^4 after reshock, indicating that the transition criterion of Dimotakis (2000) is also suitable for the convergent RM turbulence. One physical explanation is that small turbulent scales cannot feel the effect of geometric curvature.

The scaling-law exponents of the p -order structure functions, defined as $S_p(r_\theta) = \langle (|\xi(x+r_\theta) - \xi(x)|)^p \rangle$, at moments after reshock for case 1 (results for cases 2 and 3 can be found in the Supplemental file), are depicted in figure 7, where the Kolmogorov–Obukhov–Corrsin (KOC) exponent $\zeta_p = p/3$ is also provided for comparison. The exponents are obtained by linearly fitting the experimental data (see inset of figure 7) near Taylor microscale. For a short time after reshock (0.43 ms), the low-order exponents match the KOC prediction well, while the high-order ones

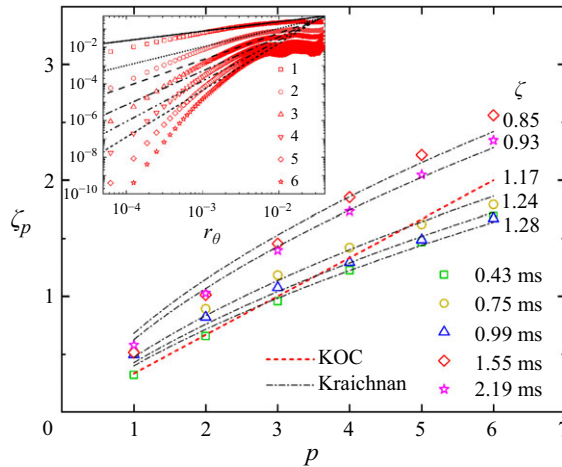


Figure 7. Scaling-law exponents of p -order structure functions.

present an evident discrepancy. As time progresses, the exponent of each order structure function increases, which we interpret as an indication of RM turbulence decay. Specifically, following reshock, fluid mixing becomes more homogeneous and thus turbulent fluctuations are reduced, especially at smaller scales, resulting in larger structure function exponents. Kraichnan (1994) proposed an anomalous scaling theory, given by $\zeta_p = 1/2\sqrt{6p(2 - \zeta) + (1 + \zeta)^2} - ((1/2)(1 + \zeta))$, where the parameter ζ ranges from 0 to 2. The present data match well with Kraichnan’s theory provided appropriate values of ζ . It is found that flow homogenization correlates with an increased ζ parameter, reflecting the physical meaning of the model. While Kraichnan’s theory was developed for isotropic turbulence at very high Reynolds numbers, there are several important considerations that support the partial applicability of this theory to our case. First, the RM turbulence, although globally inhomogeneous and anisotropic, exhibits local isotropy in the mixing plane perpendicular to the shock propagation direction (Zhou 2001; Zhou *et al.* 2003a). This local isotropy provides a basis for applying theories developed for isotropic turbulence. Second, during turbulent transition in RM instability, a significant decoupling occurs between the energy-containing range and the dissipation range, establishing an inertial subrange. This decoupling reduces Reynolds number dependence, although higher Reynolds numbers do yield a broader inertial subrange (Dimotakis 2000; Zhou *et al.* 2019). Despite these, we acknowledge the necessity of cautious interpretation of these comparisons due to the fundamental differences between idealized homogeneous isotropic turbulence (HIT) and the experimental conditions in our study.

The PLIF diagnostics can only capture 2-D data, and thus the energy spectrum and structure function reported in this work are calculated in a direction parallel to the mixing layer rather than using 3-D data. This raises the question of whether turbulent fluctuations in the spanwise direction differ statistically from those in the azimuthal direction. As far as we know, this issue has not been addressed through experiments since measuring the flow in the spanwise direction is challenging. However, previous numerical studies (Ge *et al.* 2020) on convergent RM turbulence have shown that after reshock, the azimuthal and spanwise energy spectra become nearly identical, as the reflected shock can effectively eliminate initial interface features. This supports the analyses in this work.

4. Conclusions

This work realizes the first quantitative measurements of the convergent RM turbulence in a semi-annular shock tube using time-resolved PLIF diagnostics. This is achieved by using the semi-structured shock tube, which greatly facilitates the arrangement of optical path required for PLIF measurement, along with a novel interface formation technique that significantly enhances the reproducibility and reliability of RM turbulence experiment. Evolutions of fine-scale structures from linear to turbulent mixing stages are clearly captured by PLIF. It is found that geometric curvature produces a significant influence on the evolution of large-scale structures. Specifically, after reshock, the mixing width has a linear growth rate more than twice the rate in a planar geometry. Also, due to geometric constraint, the mixing width does not present a power-law growth at late stages as in planar RM turbulence. However, the small-scale dynamics seems to be independent of the geometric curvature. Therefore, the transition criterion for planar RM turbulence is also suitable for the convergent counterpart. The reshock greatly enhances the scale separation level and also increases the flow Reynolds number, thereby leading to a quick transition to turbulent mixing. The present findings demonstrate that turbulence models could be developed for the RM turbulence, irrespective of the flow geometry. We emphasize that the present findings are specific to the parametric space explored in this work. In future studies, we plan to expand the universality of these results by investigating convergent RM turbulence under various initial conditions. Particularly, we are developing a convergent shock tube with adjustable test section heights, which will enable us to systematically study the dimensional transition from 3-D to 2-D turbulent mixing and examine mixing characteristics under enhanced 2-D conditions.

Supplementary materials. To view supplementary material for this article, please visit <https://doi.org/10.1017/jfm.2025.59>.

Funding This work was supported by the National Natural Science Foundation of China (nos. 12388101, 12072341, 12122213), the National Key Research and Development Program of China (2022YFF0504500) and the Strategic Priority Research Program of Chinese Academy of Science (XDB1100120, XDB0500301).

Declaration of interests The authors report no conflict of interest.

REFERENCES

- BALAKUMAR, B.J., ORLICZ, G.C., TOMKINS, C.D. & PRESTRIDGE, K.P. 2008 Simultaneous particle-image velocimetry-planar laser-induced fluorescence measurements of Richtmyer–Meshkov instability growth in a gas curtain with and without reshock. *Phys. Fluids* **20** (12), 124103.
- BARNES, C.W. *et al.* 2002 Observation of mix in a compressible plasma in a convergent cylindrical geometry. *Phys. Plasmas* **9** (11), 4431–4434.
- BIAMINO, L., JOURDAN, G., MARIANI, C., HOUAS, L., VANDENBOOMGAERDE, M. & SOUFFLAND, D. 2015 On the possibility of studying the converging Richtmyer–Meshkov instability in a conventional shock tube. *Exp. Fluids* **56** (2), 1–5.
- BOFFETTA, G. & ECKE, R.E. 2012 Two-dimensional turbulence. *Annu. Rev. Fluid Mech.* **44** (1), 427–451.
- CARTER, J., PATHIKONDA, G., JIANG, N., FELVER, J.J., ROY, S. & RANJAN, D. 2019 Time-resolved measurements of turbulent mixing in shock-driven variable-density flows. *Sci. Rep.* **9** (1), 20315.
- COOK, A.W. & DIMOTAKIS, P.E. 2001 Transition stages of Rayleigh–Taylor instability between miscible fluids. *J. Fluid Mech.* **443**, 69–99.
- DIMOTAKIS, P.E. 2000 The mixing transition in turbulent flows. *J. Fluid Mech.* **409**, 69–98.
- DING, J., SI, T., CHEN, M., ZHAI, Z., LU, X. & LUO, X. 2017*a* On the interaction of a planar shock with a three-dimensional light gas cylinder. *J. Fluid Mech.* **828**, 289–317.
- DING, J., SI, T., YANG, J., LU, X., ZHAI, Z. & LUO, X. 2017*b* Measurement of a Richtmyer–Meshkov instability at an air–SF₆ interface in a semiannular shock tube. *Phys. Rev. Lett.* **119** (1), 014501.

- GE, J., ZHANG, X.T., LI, H.F. & TIAN, B.L. 2020 Late-time turbulent mixing induced by multimode Richtmyer–Meshkov instability in cylindrical geometry. *Phys. Fluids* **32** (12), 124116.
- GROOM, M. & THORNER, B. 2021 Reynolds number dependence of turbulence induced by the Richtmyer–Meshkov instability using direct numerical simulations. *J. Fluid Mech.* **908**, A31.
- HOSSEINI, S.H.R. & TAKAYAMA, K. 2005 Experimental study of Richtmyer–Meshkov instability induced by cylindrical shock waves. *Phys. Fluids* **17** (8), 084101.
- JACOBS, J.W. 1992 Shock-induced mixing of a light-gas cylinder. *J. Fluid Mech.* **234** (-1), 629–649.
- KRAICHNAN, R.H. 1994 Anomalous scaling of a randomly advected passive scalar. *Phys. Rev. Lett.* **72** (7), 1016–1019.
- LEINOV, E., MALAMUD, G., ELBAZ, Y., LEVIN, L.A., BEN-DOR, G., SHVARTS, D. & SADOT, O. 2009 Experimental and numerical investigation of the Richtmyer–Meshkov instability under re-shock conditions. *J. Fluid Mech.* **626**, 449–475.
- LINDL, J., LANDEN, O., EDWARDS, J., MOSES, E. & TEAM, N. 2014 Review of the national ignition campaign 2009–2012. *Phys. Plasmas* **21** (2), 020501.
- LOMBARDINI, M., PULLIN, D.I. & MEIRON, D.I. 2014 Turbulent mixing driven by spherical implosions. Part 1. Flow description and mixing-layer growth. *J. Fluid Mech.* **748**, 85–112.
- LUO, X., DING, J., WANG, M., ZHAI, Z. & SI, T. 2015 A semi-annular shock tube for studying cylindrically converging Richtmyer–Meshkov instability. *Phys. Fluids* **27** (9), 091702.
- LUO, X., ZHANG, F., DING, J., SI, T., YANG, J., ZHAI, Z. & WEN, C. 2018 Long-term effect of Rayleigh–Taylor stabilization on converging Richtmyer–Meshkov instability. *J. Fluid Mech.* **849**, 231–244.
- MESHKOV, E.E. 1969 Instability of the interface of two gases accelerated by a shock wave. *Fluid Dyn.* **4** (5), 101–104.
- MIKHAELIAN, K.O. 1989 Turbulent mixing generated by Rayleigh–Taylor and Richtmyer–Meshkov instabilities. *Physica D* **36** (3), 343–357.
- MOHAGHAR, M., CARTER, J., PATHIKONDA, G. & RANJAN, D. 2019 The transition to turbulence in shock-driven mixing: effects of Mach number and initial conditions. *J. Fluid Mech.* **871**, 595–635.
- NOBLE, C., AMES, A., MCCONNELL, R., OAKLEY, J., ROTHAMER, D. & BONAZZA, R. 2023 Simultaneous measurements of kinetic and scalar energy spectrum time evolution in the Richtmyer–Meshkov instability upon reshock. *J. Fluid Mech.* **975**, A39.
- NOBLE, C.D., HERZOG, J.M., AMES, A.M., OAKLEY, J., ROTHAMER, D.A. & BONAZZA, R. 2020 High speed PLIF study of the Richtmyer–Meshkov instability upon re-shock. *Physica D* **410**, 132519.
- POPE, S. 2000 *Turbulent Flows*. Cambridge University Press.
- RAYLEIGH, L. 1883 Investigation of the character of the equilibrium of an incompressible heavy fluid of variable density. *Proc. Lond. Math. Soc.* **14**, 170–177.
- RICHTMYER, R.D. 1960 Taylor instability in shock acceleration of compressible fluids. *Commun. Pure Appl. Maths* **13** (2), 297–319.
- SEWELL, E.G., FERGUSON, K.J., KRIVETS, V.V. & JACOBS, J.W. 2021 Time-resolved particle image velocimetry measurements of the turbulent Richtmyer–Meshkov instability. *J. Fluid Mech.* **917**, A41.
- TAYLOR, G. 1950 The instability of liquid surfaces when accelerated in a direction perpendicular to their planes. I. *Proc. R. Soc. Lond. A* **201** (1065), 192–196.
- THORNER, B. & ZHOU, Y. 2015 Numerical simulations of the two-dimensional multimode Richtmyer–Meshkov instability. *Phys. Plasmas* **22** (3), 032309.
- TRITSCHLER, V.K., OLSON, B.J., LELE, S.K., HICKEL, S., HU, X.Y. & ADAMS, N.A. 2014 On the Richtmyer–Meshkov instability evolving from a deterministic multimode planar interface. *J. Fluid Mech.* **755**, 429–462.
- UKAI, S., BALAKRISHNAN, K. & MENON, S. 2011 Growth rate predictions of single- and multi-mode Richtmyer–Meshkov instability with reshock. *Shock Waves* **21** (6), 533–546.
- WANG, R., SONG, Y., MA, Z., MA, D., WANG, L. & WANG, P. 2022 The transition to turbulence in rarefaction-driven Rayleigh–Taylor mixing: effects of diffuse interface. *Phys. Fluids* **34** (1), 015125.
- WEBER, C.R., HAEHN, N.S., OAKLEY, J.G., ROTHAMER, D.A. & BONAZZA, R. 2014 An experimental investigation of the turbulent mixing transition in the Richtmyer–Meshkov instability. *J. Fluid Mech.* **748**, 457–487.
- ZHOU, Y. 2001 A scaling analysis of turbulent flows driven by Rayleigh–Taylor and Richtmyer–Meshkov instabilities. *Phys. Fluids* **13** (2), 538–543.
- ZHOU, Y., CABOT, W.H. & THORNER, B. 2016 Asymptotic behavior of the mixed mass in Rayleigh–Taylor and Richtmyer–Meshkov instability induced flows. *Phys. Plasmas* **23** (5), 052712.
- ZHOU, Y., CLARK, T.T., CLARK, D.S., GAIL GLENDINNING, S., AARON SKINNER, M., HUNTINGTON, C.M. & REMINGTON, B.A. 2019 Turbulent mixing and transition criteria of flows induced by hydrodynamic instabilities. *Phys. Plasmas* **26** (8), 080901.

- ZHOU, Y., REMINGTON, B.A., ROBey, H.F., COOK, A.W., GLENDINNING, S.G., DIMITS, A. & ELIASON, D. 2003*a* Progress in understanding turbulent mixing induced by Rayleigh–Taylor and Richtmyer–Meshkov instabilities. *Phys. Plasmas* **10** (5), 1883–1896.
- ZHOU, Y., ROBey, H.F. & BUCKINGHAM, A.C. 2003*b* Onset of turbulence in accelerated high-Reynolds-number flow. *Phys. Rev. E* **67** (5), 056305.